Field-induced magnetic states in the metallic rare-earth layered triangular antiferromagnet $TbAuAl_4Ge_2$

Ian A. Leahy,[1] Keke Feng,[2] Roei Dery,[3] Ryan Baumbach,[2,4] and Minhyea Lee[1]
[1]*Department of Physics, University of Colorado, Boulder, Colorado 80309, USA*
[2]*Department of Physics, Florida State University, Tallahassee, Florida 32306, USA*
[3]*Department of Physics, Cornell University, Ithaca, New York 14853, USA*
[4]*National High Magnetic Field Laboratory, Tallahassee, Florida 32310, USA*

(Received 27 June 2022; accepted 31 August 2022; published 22 September 2022)

Magnetic frustration in metallic rare- earth lanthanides (*Ln*) with $4f$ electrons is crucial for producing interesting magnetic phases with high magnetic anisotropy where intertwined charge and spin degrees of freedom lead to novel phenomena. Here we report on the magnetic, thermodynamic, and electrical transport properties of $TbAuAl_4Ge_2$. Tb ions form two-dimensional triangular lattice layers which stack along the crystalline c axis. The magnetic phase diagram reveals multiple nearly degenerate ordered states upon applying field along the magnetically easy ab-plane before saturation. The magnetoresistance in this configuration exhibits intricate field dependence that closely follows that of the magnetization while the specific heat reveals a region of highly enhanced entropy, suggesting the possibility of a nontrivial spin textured phase. For fields applied along the c axis (hard axis), we find linear magnetoresistance over a wide range of fields. We compare the magnetic properties and magnetoresistance with an isostructural $GdAuAl_4Ge_2$ single crystal. These results identify $TbAuAl_4Ge_2$ as an environment for complex quantum spin states and pave the way for further investigations of the broader $LnAuAl_4Ge_2$ family of materials.

DOI: 10.1103/PhysRevB.106.094426

I. INTRODUCTION

Geometrically frustrated lattices (e.g., triangular, Kagome, Shastry-Sutherland, and pyrochlore) continue to attract interest because they host a variety of strongly correlated quantum phases [1,2]. The simplest examples are electronic insulators, where lattice-based frustration is not disrupted by coupling between charge and spin degrees of freedom. Beyond this, a variety of frustration-induced effects have been discussed in metallic magnets, including flat bands [3,4], quantum Hall effects in kagome systems [5], and exotic superconductivity [6]. Among such materials, f-electron metals are known for hosting novel phenomena where correlation effects manifest in diverse ways [7–9].

Recent investigations of the centrosymmetric triangular lattice magnets Gd_2PdSi_3 [10] and $Gd_3Ru_4Al_{12}$ [11] have shown topological Hall effects associated with skyrmion-lattice-like spin textures in the absence of Dzyaloshinskii-Moriya interactions [12]. Theoretical studies have ascribed these behaviors to the competition among the Ruderman-Kittel-Kasuya-Yosida (RKKY) interaction, the Kondo effect, and the strength of the geometric frustration [13–15]. More broadly, the interactions between rare-earth magnetic ions and conduction electrons provide a unique route for realizing strong electronic correlation effects [2,8,16]. Understanding these effects is key to uncovering many other novel phenomena.

Here we present the magnetic and electrical properties of metallic $TbAuAl_4Ge_2$ as a function of magnetic field and temperature. $TbAuAl_4Ge_2$ crystallizes in a rhombohedral structure with staggered triangular nets of Tb^{3+} ions as shown in Fig. 1(a). Single ions of Tb^{3+} have total angular moment $J = 6$ ($L = 3$ and $S = 3$). We study the magnetoresistance (MR) and find starkly contrasting behavior for fields applied parallel to the Tb layers ($H \parallel ab$) or perpendicular to the Tb layers ($H \parallel c$). Bulk magnetization, heat capacity, and electrical transport measurements reveal highly anisotropic and complex magnetic ordering with several distinct regions in the temperature-magnetic field phase space. In particular, we observe nearly degenerate ordered ground states for fields applied along the magnetically easy ab-plane. While this behavior is not unusual for f-electron metals, an analysis of the specific heat uncovers a region of enhanced magnetic entropy in some of these phases, which implies the presence of nontrivial spin textures similar to those seen for the prototypical skyrmion lattice systems MnSi [17] and MnGe [18]. For fields applied along the magnetically hard c axis, low-temperature electrical transport measurements additionally uncover linear magnetoresistance over a wide range of fields. Such behavior is typically associated with topological band structures [19,20] or partial gapping of the Fermi surfaces by density waves [21,22]. Finally, we compare the MR results and magnetic properties with those in the isostructural $GdAuAl_4Ge_2$, which shows similar behavior for fields applied along and perpendicular to the Gd layers. Our results invite further investigations of $TbAuAl_4Ge_2$ to expose the magnetic order parameters and their impact on electronic quantities. We anticipate that the broader $LnAuAl_4Ge_2$ family of materials

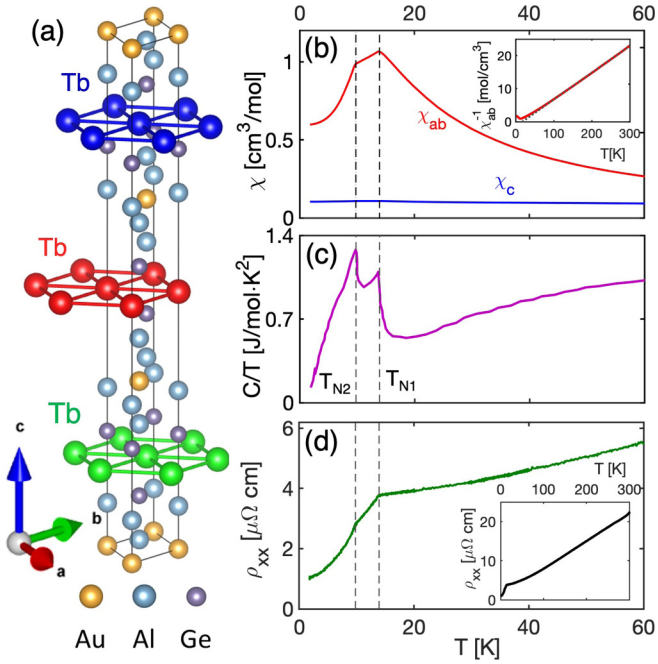

FIG. 1. (a) Crystal structure of $TbAuAl_4Ge_2$. Tb ions form a 2D triangular lattice with layers stacked along the c axis separated by approximately 1.1 nm. (b) Temperature-dependent magnetic susceptibility measured at $\mu_0 H = 0.5$ T for $H \parallel ab$ (χ_{ab}) and $H \parallel c$ (χ_c). The inset displays the Curie-Weiss fit of χ_{ab}^{-1} above 150 K, yielding the effective magnetic moments $9.9\mu_B$/Tb. Temperature dependence of specific heat (c) and resistivity (d) at zero field are shown, respectively. Two magnetic transitions at $T_{N1} = 13.9$ K and $T_{N2} = 9.8$ K are indicated with broken vertical lines in [(b)–(d)].

will provide a new reservoir for related quantum spin states and novel phenomena.

II. EXPERIMENTAL DETAILS

Single crystals of $TbAuAl_4Ge_2$ and $GdAuAl_4Ge_2$ were grown using a molten aluminum flux method. Details on the crystal growth conditions are found elsewhere [23,24]. The space group of the crystals was confirmed $R\bar{3}m$, using powder x-ray diffraction measurements with a Cu $K\alpha$ source. Detailed structure analysis and comparison with other lanthanide element substitutions are reported in Ref. [24]. Specimens were aligned by single-crystal x-ray diffraction measurements with graphite monochromated Mo $K\alpha$ radiation. Temperature and magnetic field-dependent magnetization measurements were performed for $T = 1.8$–300 K and $\mu_0 H = 0$–7 T using a Quantum Design magnetic properties measurement system. Specific heat measurements were performed for $T = 1.8$–70 K and $\mu_0 H = 0$–5 T using a Quantum Design physical properties measurement system using a conventional thermal relaxation technique. Electrical transport measurements were performed using a standard low-frequency ac technique with a four-probe configuration in a commercial cryostat and superconducting magnet. The dimensions of the transport samples used here are typically $\sim 0.7 \times 0.3 \times 0.2$ mm^3 for $TbAuAl_4Ge_2$ and $\sim 0.5 \times 0.2 \times 0.1$ mm^3 for $GdAuAl_4Ge_2$. Field symmetrization is performed on time-reversed field sweeps (up and down) to calculate the longitudinal resistivity (ρ) and eliminate electrical pickup from contact misalignment. The magnetic field was applied along either the ab-plane ($H \parallel ab$) or the c axis ($H \parallel c$) as in the magnetization measurements, with the current applied in the ⟨100⟩ Tb layer of the ab-plane. For both cases, the current lies within the ab-plane and perpendicular to the field direction.

As pointed out in earlier works (e.g., Ref. [25]), due to the large size of magnetic moments of rare-earth magnets, it is crucial to take into account the shape-dependent demagnetization effect. This is especially important when the different shapes of samples were used in magnetization and resistivity measurements as we did here, and the characteristic fields from two measurements were used to determine the phase boundaries in the temperature-field phase diagram. We will discuss this further in the next section. From here on, $\mu_0 H$ refers to applied field, while the demagnetization-corrected field (B_{int}) is used for some of our data, where the identification and comparison of the characteristic fields are necessary.

III. RESULTS AND DISCUSSION

A. In-plane magnetization and magnetic phase diagram of $TbAuAl_4Ge_2$

Figure 1(a) shows the unit cell of $TbAuAl_4Ge_2$, where the Tb ions form staggered layers of two-dimensional triangular nets that are stacked along the c axis The Tb layers are spaced approximately 1.1 nm apart from one another and the in-plane nearest Tb neighbor distance is found at 0.42 nm [24]. The triangular arrangement of Tb ions is the basis of the geometric conditions for magnetic frustration, where the long-range RKKY interaction and crystal electric field splitting of the Hund's rule multiplet of Tb^{3+} are also anticipated to play an important role, adding complexity to the landscape of relevant energy scales. As shown in Fig. 1(b), $\chi(T)$ shows strong anisotropy for magnetic fields applied in the ab-plane (χ_{ab}) and along the c axis (χ_c), where $\chi_{ab} \gg \chi_c$. A Curie-Weiss fit to χ_{ab} for $T > 200$ K yields a Curie-Weiss temperature $\Theta_{\text{CW}} = 18$ K and an effective magnetic moment $\mu_{\text{eff}} = 9.9\mu_B$/Tb, in good agreement with the calculated moment value of single-ion Tb^{3+}, $9.7\mu_B$. Two antiferromagneticlike orderings are identified by the pronounced cusps in $\chi_{ab}(T)$ at $T_{N1} = 13.9$ K and $T_{N2} = 9.8$ K, as marked with vertical dashed lines. Both transitions at T_{N1} and T_{N2} are aligned with peaks in the specific heat as a function of temperature $C(T)$ measured at zero field [panel (c)]. In the zero-field resistivity $\rho(T)$ [panel (d)], the magnetic ordering appears as cusps corresponding to a reduction in scattering of conduction electrons upon ordering.

To further distinguish between different ordered states, we plot the isothermal field-dependent magnetization for $H \parallel ab$ (M_{ab}) [Fig. 2(a)]. The saturated magnetization at $T = 1.8$ K reaches $M_{\text{sat}} \approx 8.3\mu_B$/Tb at the internal field $B_{\text{int}} \geqslant 3.8$ T, where M_{ab} begins to slowly increase to approach the value of free Tb^{3+} ion moment, $9.7\mu_B$/Tb, corresponding to the total angular momentum $J = 6$. M_c in $H \parallel c$ configuration increases linearly and only reaches $1.25\mu_B$/Tb at $\mu_0 H = 7$ T and the slope of $\frac{dM_c}{dH}$ shows little temperature dependence.

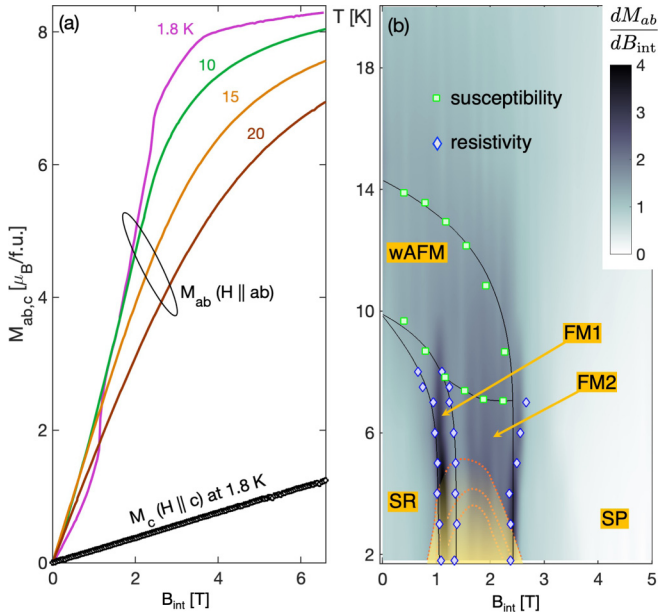

FIG. 2. (a) M_{ab} (solid lines) of $TbAuAl_4Ge_2$ with field applied along the *ab*-plane are plotted as a function of the demagnetization-effect-corrected internal field $B_{\rm int}$. At $T = 1.8$ K, M_{ab} nearly saturates at $8.3\mu_B$/Tb, making the *ab*-plane the magnetic easy plane. For comparison, M_c with $H \parallel c$ at 1.8 K is displayed as black circles. M_c increases linearly to $1.7\mu_B$/Tb at 7 T with no obvious features present. (b) Phase diagram of $TbAuAl_4Ge_2$. The color bar represents the magnitude of $dM_{ab}/dB_{\rm int}$, which follows the peak and kink positions of susceptibility and magnetoresistance. The yellow-shaded area is adopted from the specific heat data, where the magnetic contribution to the specific heat and hence magnetic entropy, displays significant enhancement (see Sec. III B). Black lines are used as a guide.

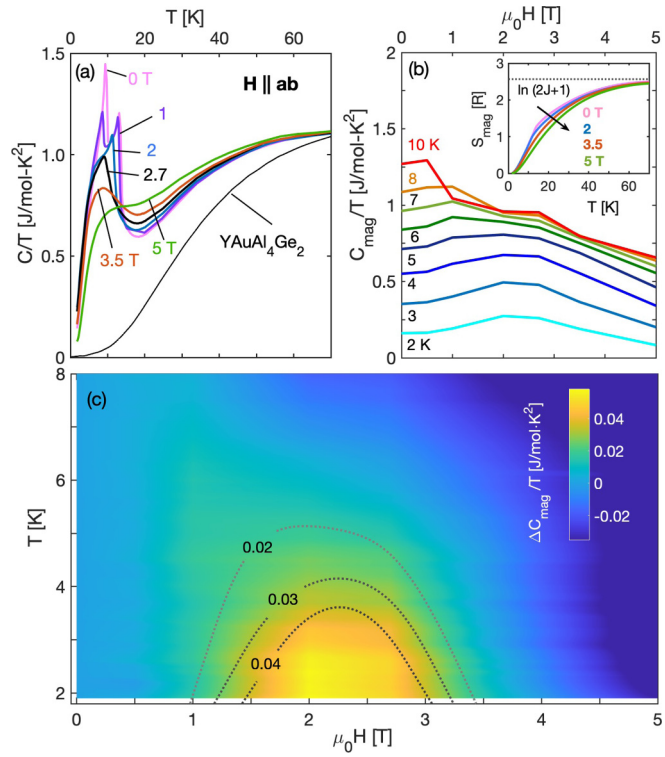

FIG. 3. (a) T dependence of C/T at different fixed fields applied along the *ab*-plane. For 0 T, two transitions marked by peaks are visible at $T_{\rm N1}$ and $T_{\rm N2}$ which become broadened with field. (b) The magnetic field dependence of $C_{\rm mag}/T$ plotted at $T = 2$–10 K in 1 K increments. A shallow maximum in $C_{\rm mag}(H)$ fades away in $T \geqslant 6$ K. Inset: Magnetic entropy, $S_{\rm mag}(T)$, at different fixed fields calculated using $\partial S_{\rm mag}/\partial T = C_{\rm mag}/T$. For all fields, $S_{\rm mag}$ converges towards $R\ln(2J+1)$, where $J = 6$ for the total angular momentum of Tb^{3+}. (c) $\Delta C_{\rm mag}(H)/T$ defined as $[C_{\rm mag}(H) - C_{\rm mag}(H=0)]/T$ is plotted in color in H-T space, which visualizes the area of enhanced $\Delta C_{\rm mag}$ centered on the low T region of FM1 and FM2 states.

For $T < T_{\rm N2}$, M_{ab} displays distinct features that indicate a series of field-induced transitions. Combined with χ_{ab} we generate a phase diagram with four distinct regions: (i) the spin rotation region (SR), where M_{ab} monotonically increases with increasing H; (ii) the first ferromagnetic region (FM1), which is bounded by a step-ike increase of M_{ab} at $B_{\rm int} = 1.0$ T and a subtle inflection point at around 1.4 T; (iii) the second ferromagnetic region (FM2), where the field derivative of M_{ab} remains larger before abruptly decreasing at $B_{\rm int} = 2.4$ T; and (iv) and the spin-polarized state (SP) characterized with mostly saturated M_{ab} with an abruptly reduced $\frac{dM_{ab}}{dB_{\rm int}}$ as field increases. The color scale of Fig. 2(b) shows the magnitude of $\frac{dM_{ab}}{dB_{\rm int}}$ overlaid with the characteristic field scales marked from $\chi_{ab}(T)$ at different fields (squares) and from $\rho(B_{\rm int})$ at different temperatures (diamonds). The features in resistivity naturally follow the phase boundaries described above, which will be discussed further in Sec. III C 1. In $T_{\rm N1} < T < T_{\rm N2}$, two different magnetic states are distinguished only by the locations of two cusps in $\chi_{ab}(T)$ at different fields, which is referred as a weakly antiferromagnetic (wAFM) state [24]. The yellow-shaded area extending across the low-temperature region of FM1 and FM2 is derived from the region of elevated magnetic heat capacity (and thus magnetic entropy). We will discuss this in the next section.

B. Specific heat of $TbAuAl_4Ge_2$

Figure 3(a) shows the plot of specific heat $C(T)$ at different fields applied along the *ab*-plane. At zero field, two transitions at $T_{\rm N1}$ and $T_{\rm N2}$ are marked by two peaks. Both peaks move to lower temperatures T with increasing field but the peak at $T_{\rm N2}$ is completely suppressed by $\mu_0 H = 2$ T. Enhancement of C/T in higher temperature ($T > T_{\rm N1}$) persists for all fields, which makes it difficult to observe the phase boundaries at FM1 and FM2. $C(T)$ of the nonmagnetic analog of $YAuAl_4Ge_2$ is shown as well, which was used to obtain the magnetic contribution $C_{\rm mag} = C - C_{\rm YAAG}$. In Fig. 3(b) we plot $C_{\rm mag}(H)/T$ at several fixed temperatures: a substantial enhancement of $C_{\rm mag}(H)/T$ emerges in the field range corresponding to FM1 and FM2 for $T < 6$ K.

In the inset of panel (b) we plot $S_{\rm mag}(T)$, calculated from $S_{\rm mag}(T) = \int C_{\rm mag}/T\, dT$. $S_{\rm mag}(T)$ reaches the value 20.7 J/mol K at 70 K, asymptotically approaching the expected value for the total angular momentum $J = 6$ for Tb ion multiplet $R\log(2J+1) = 2.56R \approx 21.3$ J/mol K, where R refers to the gas constant. This corresponds to full occupation of all angular momentum multiplets ($2J + 1 = 13$ for Tb ions), which has been reported in other RE magnetic

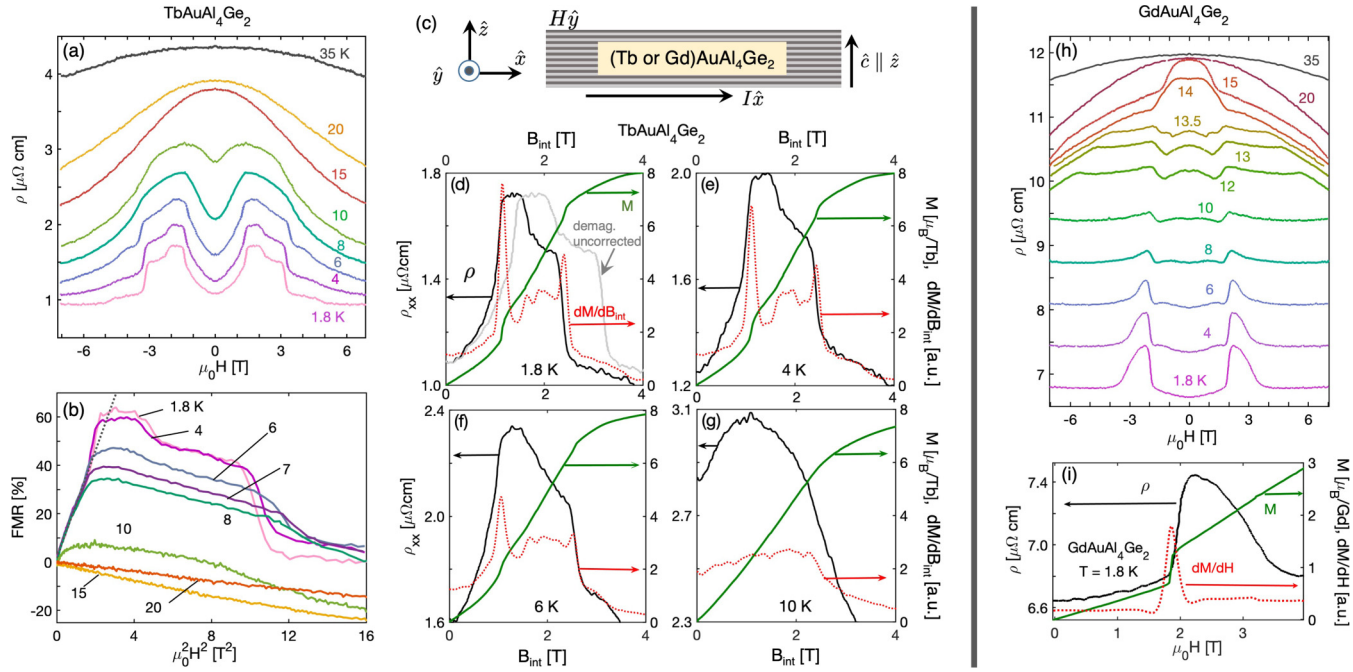

FIG. 4. (a) The schematic diagram of the MR measurement in the $H \parallel ab$ configuration: current I and field H are both in the ab-plane but perpendicular as shown, i.e., $I\hat{x} \parallel \langle 100 \rangle$ and applied field $H\hat{y}$. (b) MR measured at different fixed temperatures from 1.8 to 35 K. (c) The fractional MR plotted against H^2, revealing the initial increase is due to orbital MR where the charge carrier's motion is slicing through the Tb layers. The low-field linear slope (dotted line) shows little T dependence until the temperature reaches T_{N2}. (d)–(g) ρ, M_{ab}, and its derivative as a function of the demagnetization corrected field (B_{int}) are compared at $T = 1.8$, 4, 6, and 10 K, respectively. In panel (d), the light-gray line stands for ρ without the demagnetization correction, of which the characteristic fields are far from alignment to what were from M_{ab} or its derivative. (h) The MR (H) of $GdAuAl_4Ge_2$ in the same geometry is plotted at different fixed temperatures. (i) Comparison of $\rho(H)$, $M_{ab}(H)$, and $\frac{dM}{dH}$ in $GdAuAl_4Ge_2$ at $T = 1.8$ K. Note that MR decreases with field, even without a saturation of magnetization.

compounds [24,26,27]. This implies that all 13 eigenstates, with or without degeneracy in the crystal electric field (CEF) levels, are thermally accessible and equally populated for $T \geqslant 70$ K. In other words, all CEF levels lie below ~6 meV. Such low energy scales are expected to have little interference with the Fermi surface properties, but are likely to influence the magnetic energetics among the local Tb moments in the ordered states, potentially contributing to the complexity of the T-H phase diagram.

In order to highlight the effect of the magnetic field on the specific heat, we define $\Delta C_{mag}(T,H) \equiv C_{mag}(H,T) - C_{mag}(H=0)$ and plot $\Delta C_{mag}/T$ in color scale as a function of H and T, as shown in Fig. 3(c). We note that $C_{mag}/T = \partial S_{mag}/\partial T$, so a peak in $\Delta C_{mag}(H)/T$ corresponds to excess magnetic entropy S_{mag} caused by the applied field.

The dotted lines show contours of $\Delta C_{mag}/T$ as it decreases with increasing temperature. These contours are also displayed in our phase diagram in Fig. 2(b). For $T < 4$ K, we observe a large enhancement of ΔC_{mag} that begins at the FM1 region, is centered at the beginning of the FM2 region, and terminates at the beginning of the SP region. This suggests that the ordered state in this region has additional internal degrees of freedom compared to the surrounding areas, which has been observed in other rare-earth (RE) metallic compounds [9,15]. Similar behavior was seen for the prototypical skyrmion lattice material MnSi [17] as well as in MnGe as an enhancement of the field-dependent thermopower [18]. The enhancement of ΔC_{mag} suggests the formation of non-trivial spin textures such as skyrmions or topological bubbles [28–30] in this region of the phase diagram.

C. Magnetoresistance

1. H ∥ ab

Next, we investigate the field dependence of the MR of $TbAuAl_4Ge_2$ (Tb1142) in the $H \parallel ab$ configuration. The measurement geometry is illustrated in Fig. 4(a): the current flows along $\hat{x}$ and the field is applied along $\hat{y}$. The xy plane lies within the ab-plane of Tb1142 with $\hat{x} \parallel \langle 100 \rangle$ and $\hat{z}$ parallel to the c axis. The voltage contacts are separated along $\hat{x}$.

Figure 4(b) shows the magnetoresistance for Tb1142 at several fixed temperatures for $H \parallel ab$. Starting from $T = 1.8$ K, $\rho(H)$ exhibits a quadratic rise as a function of H in the low-field SR region, consistent with conventional orbital MR. To obtain further insight we plot the fractional MR (FMR) as a function of H^2, where the FMR is defined as $\frac{\Delta\rho(H)}{\rho_0} \times 100\%$, with $\rho_0 = \rho(H=0)$ and $\Delta\rho(H) = \rho(H) - \rho_0$. The quadratic dependence in low field persists in $T \lesssim T_{N2}$, where the slope marked with a dashed line remains unchanged. We calculate the effective carrier mobility from this slope paired with the carrier density estimated from the high-field Hall resistivity to find $\nu \approx 4.7 \times 10^4$ cm^2/V s, which is consistent with the measured low resistivity. In this particular measurement configuration the carrier cyclotron motion lies in the xz plane [Fig. 4(a)], and thus, for a spherical Fermi surface, we

estimate the cyclotron radius $r_C = \frac{mv_F}{e\mu_0 H}$ to be on the order of a few hundreds of nanometers, at $\mu_0 H = 2$ T, which corresponds to humdreds of Tb layers. Hence, we expect that the interlayer ordering pattern would make a considerable impact on the MR in addition to the ordering within individual Tb layers. A detailed investigation on the properties of magnetic ordering (e.g., neutron scattering) would shed more light on this.

Increasing the field further, we observe some detailed structure consisting of a plateau followed by slow and steplike decreases alternating in the FM1 and FM2 regions. Upon entering the SP region, $\rho(H)$ gradually decreases [as $M_{ab}(H)$ increases] as the magnetic moments begin to uniformly align with the applied field. The spins are polarizing but are not fully polarized and the field continues to raise the magnetization and lower the magnetoresistance suppressing spin fluctuations.

In panels Figs. 4(d)–4(g), we compare the detailed features of ρ (the left y axis), M_{ab}, and its derivatives (the right y axis) as a function of the demagnetization-corrected internal field (B_{int}) at $T = 1.8$, 4, 6, and 10 K, respectively. For $T = 1.8$ K [panel (d)], as the field increases from zero the curvature of $\rho(H)$ becomes stiffer than H^2 to reach a plateau, followed by subsequent decreases with two sharp drops. The characteristic fields of all three quantities are found well aligned in all panels of (d)–(g), only when the demagnetization effect is properly corrected: the field dependence of ρ without the correction is shown in panel (d) with the light-gray line of which alignments of the characteristic fields from M_{ab} and $\frac{dM}{dB_{\text{int}}}$ are poor. The field locations of the plateau and two drops are marked in diamond symbols in Fig. 2(b). These points coincide with features in $\frac{dM}{dB_{\text{int}}}$ and help to highlight the FM1 and FM2 regions in the phase diagram. All features in both $\rho(B_{\text{int}})$ and $M_{ab}(B_{\text{int}})$ begin to smear with increasing temperature above 6 K and are mostly wiped out by $T = 10$ K, just above T_{N1}. Unlike the orbital MR induced by the Lorentz force in the SR region, the increases and decreases in MR in FM1 and FM2 are likely to arise from the RKKY interaction of carriers with the magnetic state, reflecting a field-dependent change in the carrier relaxation time, τ. The field dependence of $\tau(H)$ is determined by the interaction between the Tb moments and conduction electrons via a contact exchange interaction, $J_{\text{c-f}}$ [31]. From the estimation of r_C at low field, $\tau(H)$ is expected to depend on the ordering arrangement both within and between Tb layers.

For $T > T_{\text{N2}}$, Tb1142 enters the wAFM region where the suppression of spin scattering by field becomes more effective as the resistivity at high field is much lower than ρ_0 [panel (g)]. This indicates strong spin fluctuations at zero field and hence a weakly ordered state. In this region, the spin interactions responsible for generating the anomalies at low temperatures are destabilized by thermally enhanced spin fluctuations and geometric frustration.

2. *Comparison with* $GdAuAl_4Ge_2$

To gain insight, we compare the in-plane field dependence of the MR with that of isostructural $GdAuAl_4Ge_2$ (Gd1142). The Gd analog exhibits three subsequent magnetic orderings at $T_{N1,2,3} = 17.8$, 15.6, and 13.6 K, identified by features in $\chi_{ab}(T)$ (for details, see Ref. [24]). Unlike Tb1142, the magnetization of Gd1142 reveals significantly less anisotropy. This smaller anisotropy in Gd1142 is due to the zero orbital angular moment of the Gd^{3+} ions (with $J = 7/2$, $L = 0$, and $S = 7/2$). At $T = 1.8$ K, the M_{ab} of Gd1142 does not get saturated up to $\mu_0 H = 7$ T.

Despite the smaller magnetic anisotropy, Fig. 4(h) shows a featured $\rho(H)$ for $H \parallel ab$ that evolves as a function of temperature. Below 10 K, the field dependence for Gd1142 is simpler yet similar to that of Tb1142. The multiple-featured horn shape observed in Tb1142 is replaced with a smooth, featureless horn in Gd1142. In both samples, the evolution with increasing temperature is similar. As in Tb1142, the onset of the hornlike region in Gd1142 corresponds to a metamagneticlike increase in $M_{ab}(H)$ at 1.9 T (at 1.8 K). We highlight the coincidence of the sharp magnetization increase and the onset of the horn in the MR at 1.8 K in Fig. 4(i). Unlike Tb1142, there is only one sharp magnetization increase in Gd1142 which corresponds to the onset of the horn feature. Above 10 K, the low-field MR for Gd1142 develops a concave curvature that narrows in field range with increasing temperature. Above $T = 12$ K, an additional shoulderlike feature followed by negative MR emerges, gradually transitioning to negative, parabolic MR at all fields above $T_{\text{N3}} = 17.8$ K. At these elevated temperatures, none of the observed subtle features in Gd1142 are reflected in its magnetization. This may indicate that the MR is more sensitive to subtle rearrangements in the magnetic states that leave the bulk magnetization unaltered.

The MRs for $H \parallel ab$ in both samples bear a striking similarity. Above the ordering temperature, applied fields reduce scattering and decrease the resistivity. Below their ordering temperatures, both samples show an MR with a horn feature that coincides with a sharp metamagneticlike transition [24]. This feature is present at low temperatures and disappears before reaching the highest ordering temperature and is embedded with subtle changes likely corresponding to intermediate magnetic states. It is also interesting to compare the high-field behavior at 1.8 K in Gd1142 [panel (i)] and Tb1142 [panel (d)]: The field dependence of MR in Gd1142 displays a decrease to be flattened even in the absence of the saturation of magnetization and the field-independent MR occurs at a much higher field than where $\frac{dM_{ab}}{dB_{\text{int}}}$ spikes. This implies that Tb1142 undergoes much stronger spin fluctuations and hence higher degrees of magnetic frustration than Gd1142, which may be related to the different angular momentum states of two ions. Based on our observations in Tb1142 and Gd1142, we expect the broader family of Ln1142 compounds to show varied, interesting correlated magnetic and electrical behavior. The intricate and diverse field dependence of the MR and its origin is of great interest in order to understand the RKKY interaction for different ions with distinct total angular momentum states.

3. $H \parallel c$

In the $H \parallel c$ configuration with $I \parallel \hat{x}$ (measuring the same longitudinal resistivity), we observe starkly contrasting behavior. Figures 5(a) and 5(b) display the field dependence of the MR for Tb1142 and Gd1142, respectively. In Tb1142, for all measured temperatures to 20 K the MR with $H \parallel c$

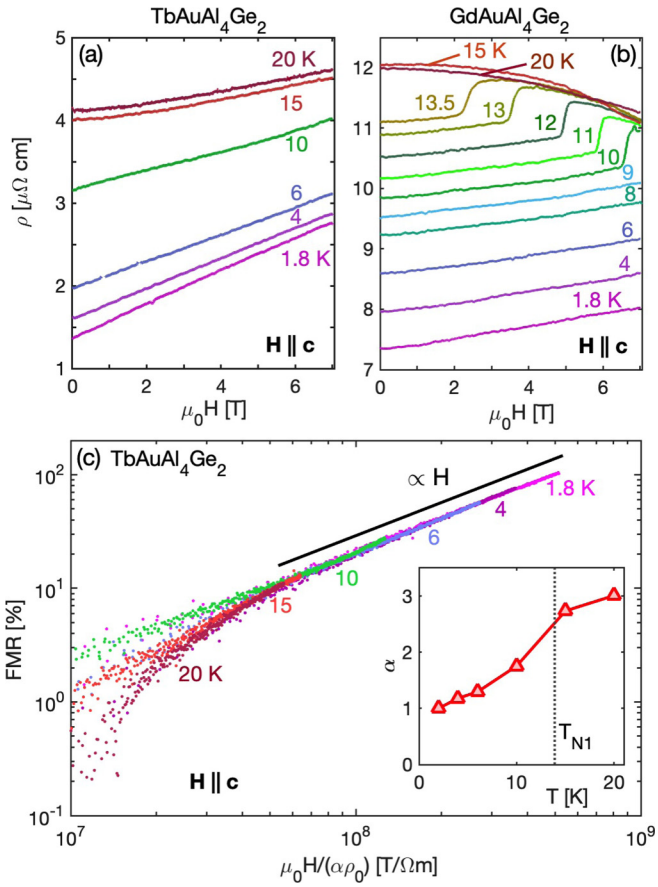

FIG. 5. (a) Positive MR(H) of $TbAuAl_4Ge_2$ in the $H \parallel c$ configuration, where the current direction remains along $\hat{x}$ but the field is rotated so that $H \parallel \hat{c}$ [Fig. 4(a)]. MR exhibits strikingly linear H dependence, below T_{N2}. (b) MR(H) of $GdAuAl_4Ge_2$ with $H \parallel c$. The similar linear positive MR persists up to 10 K. At 10 K, a sharp, steplike increase occurs at high field (H_{Kc}) and moves toward smaller fields with increasing temperature. Above $T_{N3} = 13.6$ K, the MR becomes negative and parabolic. (c) Modified Kohler plot of the FMR vs $\mu_0 H/(\alpha\rho_0)$ for $TbAuAl_4Ge_2$, where an additional scaling factor, α, is introduced to scale the zero-field resistivity and collapse the data. The inset plots this scaling factor vs temperature. As T is lowered, α begins to decrease below T_{N1} and approach unity below T_{N2}, indicating a change of the scattering mechanism in $T_{N2} < T < T_{N1}$.

remains positive. For $T = 1.8$–6 K, the MR is strictly field linear. Above T_{N2}, the low-field MR starts to develop nonlinear curvature, but remains positive.

In Gd1142, we observe similar H-linear MR for $T = 1.8$–9 K. Between 10 and 13.5 K the MR remains linear below a steplike transition that appears at high field (H_{Kc}) and moves towards lower fields with increasing temperatures. We note that no corresponding feature was observed in $M_c(H)$ at H_{Kc} (data shown in Ref. [24]). For 15 K and above, the MR turns negative (merging with the behavior above the emergent step feature).

To disentangle the carrier scattering mechanisms when $H \parallel c$ in Tb1142, we adopt a phenomenological modification to the standard Kohler plot [Fig. 5(c)]. We introduce a field-independent but T-dependent scaling factor, $\alpha(T)$, which multiplies $\rho_0(T)$ to cause all MR curves to collapse. The scaling factor remains near 1 for $T < T_{N2}$ where linear MR is most prominent, then rapidly increases towards a value of 3 as T increases through T_{N1}. This is interpreted as a threefold increase in scattering with field in the higher T wAFM region, compared to below the ordering temperature.

While the mechanism responsible for the linear MR in Gd1142 and Tb1142 is not immediately obvious, it is clear that the linear MR is not directly correlated to the spin degree of freedom. Gd1142 and Tb1142 host different degrees of anisotropy with correspondingly different magnetizations for $H \parallel c$ (for Tb1142, M_{ab} is more than five times larger than M_c, while for Gd1142 it is only 1.4 times larger), yet both samples show similarly sized linear MR. Linear MR has been shown to originate from electronic origins as a result of certain Fermi surface [15,32,33] or band structure properties [19]. Some f-electron metallic systems are found to exhibit linear MR over large field ranges that has been connected to the modification of high curvature Fermi surfaces due to zone-folding energy gaps [16,21,22], resulting from the formation of charge or spin density waves. For Tb1142 and Gd1142, linear MR is only seen for $T < T_{N2}$, which may suggest that incommensurate AFM order may introduce gapped Fermi surface regions leading to linear MR for $H \parallel c$. Meanwhile the *ab*-plane behavior is dominated by field-induced transitions and the corresponding changes in spin scattering. Charge density wave formation has been observed in other lanthanide compounds with unambiguous signatures in the diffraction pattern as well as a shoulderlike increase of the resistivity at the Peierls transition temperature [22,34]. This motivates further studies to understand this behavior and to determine whether it is present in the chemical analogs.

IV. SUMMARY

We have reported the heat capacity and field-direction dependent magnetoresistance results in the metallic rare-earth layered triangular antiferromagnetic compound $TbAuAl_4Ge_2$. A small range of applied fields along the *ab*-plane drives the system through multiple magnetic states as reflected in the magnetoresistance and magnetization, resulting in a rich magnetic phase diagram where the energy scales of these states are narrowly separated. Simultaneously, a region of enhanced magnetic specific heat suggests the possibility of nontrivial spin textures hosted in the low-T regions of FM1 and FM2. For $H \parallel c$, positive linear MR emerges over a wide field range below the ordering temperature, which is also observed in the isostructural, more magnetically isotropic $GdAuAl_4Ge_2$. We suspect that the linear magnetoresistance is electronic in origin: one possibility is that the Fermi surface in both compounds undergoes reconstruction due to density wave physics or other electronic correlation effects. Taken together, these measurements motivate further work to clarify the details of the magnetic states in $TbAuAl_4Ge_2$, such as neutron scattering, magnetic force microscopy, or Lorentz transmission electron microscopy. It is also of interest to examine the variation of our observations, by varying the lanthanide and transition metal ions in the chemical analogs.

ACKNOWLEDGMENTS

M.L. and I.A.L were supported by the U.S. Department of Energy, Basic Energy Sciences, Materials Sciences and Engineering Division under Award No. DE-SC0021377. R.B. and K.F. were supported by the National Science Foundation through NSF DMR-1904361. R.D. acknowledges the support from the NSF Research Experiences for Undergraduates program of 2021. A portion of the electrical transport measurements were performed at the National High Magnetic Field Laboratory, which is supported by the National Science Foundation Cooperative Agreement No. DMR-1644779 and the State of Florida.

[1] L. Balents, Nature (London) **464**, 199 (2010).
[2] Q. Si and F. Steglich, Science **329**, 1161 (2010).
[3] M. Kang, S. Fang, L. Ye, H. C. Po, J. Denlinger, C. Jozwiak, A. Bostwick, E. Rotenberg, E. Kaxiras, J. G. Checkelsky, and R. Comin, Nat. Commun. **11**, 4004 (2020).
[4] M. Kang, L. Ye, S. Fang, J.-S. You, A. Levitan, M. Han, J. I. Facio, C. Jozwiak, A. Bostwick, E. Rotenberg *et al.*, Nat. Mater. **19**, 163 (2020).
[5] E. Tang, J.-W. Mei, and X.-G. Wen, Phys. Rev. Lett. **106**, 236802 (2011).
[6] B.-J. Yang, Y. B. Kim, J. Yu, and K. Park, Phys. Rev. B **77**, 104507 (2008).
[7] C. Lacroix, J. Phys. Soc. Jpn. **79**, 011008 (2010).
[8] H. v. Löhneysen, A. Rosch, M. Vojta, and P. Wölfle, Rev. Mod. Phys. **79**, 1015 (2007).
[9] K. Fushiya, T. D. Matsuda, R. Higashinaka, K. Akiyama, and Y. Aoki, J. Phys. Soc. Jpn. **83**, 113708 (2014).
[10] T. Kurumaji, T. Nakajima, M. Hirschberger, A. Kikkawa, Y. Yamasaki, H. Sagayama, H. Nakao, Y. Taguchi, T.-h. Arima, and Y. Tokura, Science **365**, 914 (2019).
[11] M. Hirschberger, T. Nakajima, S. Gao, L. Peng, A. Kikkawa, T. Kurumaji, M. Kriener, Y. Yamasaki, H. Sagayama, H. Nakao *et al.*, Nat. Commun. **10**, 5831 (2019).
[12] S. Mulbauer, B. Binz, F. Jonietz, C. Pfleiderer, A. Rosch, A. Neubauer, R. Georgii, and P. Böni, Science **323**, 915 (2009).
[13] S. Doniach, Phys. B (Amsterdam, Neth.) **91**, 231 (1977).
[14] P. T. Coleridge, J. Phys. F **17**, L79 (1987).
[15] S. Lucas, K. Grube, C.-L. Huang, A. Sakai, S. Wunderlich, E. L. Green, J. Wosnitza, V. Fritsch, P. Gegenwart, O. Stockert, and H. v.Löhneysen, Phys. Rev. Lett. **118**, 107204 (2017).
[16] S. Tsuda, C. L. Yang, Y. Shimura, K. Umeo, H. Fukuoka, Y. Yamane, T. Onimaru, T. Takabatake, N. Kikugawa, T. Terashima *et al.*, Phys. Rev. B **98**, 155147 (2018).
[17] A. Bauer, M. Garst, and C. Pfleiderer, Phys. Rev. Lett. **110**, 177207 (2013).
[18] Y. Fujishiro, N. Kanazawa, T. Shimojima, A. Nakamura, K. Ishizaka, T. Koretsune, R. Arita, A. Miyake, H. Mitamura, K. Akiba *et al.*, Nat. Commun. **9**, 408 (2018).
[19] L. Ye, T. Suzuki, C. R. Wicker, and J. G. Checkelsky, Phys. Rev. B **97**, 081108(R) (2018).
[20] I. A. Leahy, Y.-P. Lin, P. E. Siegfried, A. C. Treglia, J. C. W. Song, R. M. Nandkishore, and M. Lee, Proc. Natl. Acad. Sci. USA **115**, 10570 (2018).
[21] Y. Feng, Y. Wangb, D. M. Silevitch, J.-Q. Yan, R. Kobayashia, M. Hedo, T. Nakama, Y. Onuki, A. V. Suslov, B. Mihaila, P. B. Littlewood, and T. F. Rosenbaum, Proc. Natl. Acad. Sci. USA **116**, 11201 (2019).
[22] K. K. Kolincio, M. Roman, and T. Klimczuk, Phys. Rev. Lett. **125**, 176601 (2020).
[23] S. Zhang, N. Aryal, K. Huang, K.-W. Chen, Y. Lai, D. Graf, T. Besara, T. Siegrist, E. Manousakis, and R. E. Baumbach, Phys. Rev. Mater. **1**, 044404 (2017).
[24] K. Feng, I. A. Leahy, O. Oladehin, K. Wei, M. Lee, and R. Baumbach, arXiv:2205.14063.
[25] S. Legl, C. Krey, S. R. Dunsiger, H. A. Dabkowska, J. A. Rodriguez, G. M. Luke, and C. Pfleiderer, Phys. Rev. Lett. **109**, 047201 (2012).
[26] N. P. Raju, M. Dion, M. J. P. Gingras, T. E. Mason, and J. E. Greedan, Phys. Rev. B **59**, 14489 (1999).
[27] N. Takeda and M. Ishikawa, J. Phys. Soc. Jpn. **69**, 868 (2000).
[28] T. Shinjo, T. Okuno, R. Hassdorf, K. Shigeto, and T. Ono, Science **289**, 930 (2000).
[29] L. Vistoli, W. Wang, A. Sander, Q. Zhu, B. Casals, R. Cichelero, A. Barthélémy, S. Fusil, G. Herranz, S. Valencia *et al.*, Nat. Phys. **15**, 67 (2019).
[30] D. Wulferding, H. Kim, I. Yang, J. Jeong, K. Barros, Y. Kato, I. Martin, O. Ayala-Valenzuela, M. Lee, H. C. Choi *et al.*, Sci. Rep. **7**, 46296 (2017).
[31] L. Ye, T. Suzuki, and J. G. Checkelsky, Phys. Rev. B **95**, 174405 (2017).
[32] G. Oomi, T. Kagayama, K. Kawaguchi, P. C. Canfield, and S. L. Bud'ko, Phys. B: Condensed Matter **230-232**, 776 (1997).
[33] S. L. Bud'ko, P. C. Canfield, C. H. Mielke, and A. H. Lacerda, Phys. Rev. B **57**, 13624 (1998).
[34] M. Stavinoha, J. A. Cooley, S. G. Minasian, T. M. McQueen, S. M. Kauzlarich, C.-L. Huang, and E. Morosan, Phys. Rev. B **97**, 195146 (2018).